



Cite this: *J. Mater. Chem. A*, 2025, 13, 21683

## $\pi$ -Extended dihydrophenazine based redox responsive polymers of intrinsic microporosity†

Grazia C. Bezzu,<sup>a</sup> Beatrice Bartolomei,<sup>bc</sup> Yue Wu,<sup>a</sup> Martina Vaccaro,<sup>d</sup> Mariagiulia Longo,<sup>d</sup> Maria Penelope De Santo,<sup>e</sup> Alessio Fuoco,<sup>\*d</sup> Maurizio Prato,<sup>id \*bfg</sup> Mariolino Carta<sup>id \*a</sup> and Jacopo Dosso<sup>id \*b</sup>

Redox-switchable Polymers of Intrinsic Microporosity (PIMs) are a promising yet underexplored class of materials. Here, we introduce  $\pi$ -extended dihydrophenazine-based PIMs for gas separation. The *tert*-butyl substituted **Phen-PIM-1** stands out as a rare example of a redox-active switchable polymer with a high surface area (BET >600 m<sup>2</sup> g<sup>-1</sup>) and excellent balance of porosity, pore size, and gas selectivity. **Phen-PIM-1** is soluble in *N*-methyl pyrrolidone (NMP), enabling membrane fabrication, while the methyl-substituted **Phen-PIM-2** is insoluble, highlighting the role of bulky *tert*-butyl groups (tBu) in solubility and film formation. Gas separation studies, performed on powder (IAST), demonstrate outstanding performance, with CO<sub>2</sub>/N<sub>2</sub> selectivity up to 49. As a membrane material, **Phen-PIM-1** shows competitive separation within the Robeson upper bound for several commercially important gas pairs, proving its potential for carbon capture and molecular sieving. Furthermore, these materials exhibit efficient and reversible redox switching upon chemical stimuli, leading to marked differences in properties and enhanced selectivity. This study establishes dihydrophenazine-based PIMs as a versatile platform for developing tunable, high-performance membranes for energy and environmental applications.

Received 27th March 2025  
Accepted 2nd June 2025

DOI: 10.1039/d5ta02477c

rs.c.li/materials-a

## 1. Introduction

The development of novel porous polymeric materials is currently one of the most investigated areas of chemistry.<sup>1,2</sup> This interest arises from the great impact of such materials for applications in gas adsorption/separation,<sup>1,3,4</sup> energy storage,<sup>5–8</sup> and catalysis,<sup>9–12</sup> which are of paramount importance to tackle the climate crisis that we are currently witnessing. As such, the number of works revolving around the development of innovative Metal organic frameworks (MOFs), Covalent organic frameworks (COFs) and in general, polymeric porous materials, is constantly rising. From this point of view, polymers of

intrinsic microporosity (PIMs) have been extensively studied due to their highly promising surface areas and tunable functionalization, especially considering that many PIMs can be solution cast into membranes, and thus they can be efficiently exploited for gas separation applications. From the structural point of view, PIMs are a class of highly porous materials defined by their rigid and contorted monomeric structures, which prevent efficient chain packing and create interconnected micropores (<2 nm). Their microporosity arises from a combination of intrinsic backbone rigidity and sites of contortion, such as spiro-centers or ladder-like linkages, that disrupt dense packing.<sup>13</sup> This results in high free volume and permanent porosity without the need for post-synthetic processing. PIMs' high surface area and tunable chemistry make them ideal for gas separation, CO<sub>2</sub> capture, and membranes.<sup>14,15</sup> Post-polymerization changes and further functionalization of the PIMs' backbones are extensively used strategies to improve their potential in gas separation and adsorption applications. For example, Weng<sup>16</sup> and co-workers exploited the nitrile groups present in pre-formed PIMs to generate triazine cross-links *in situ*, leading to improved separation performance despite a reduction in porosity. Similarly, Rizzuto *et al.*<sup>17</sup> demonstrated that reducing nitrile groups in PIM-1 to primary amines significantly enhanced CO<sub>2</sub> selectivity, attributing this effect to competitive sorption interactions confirmed *via* mixed-gas studies, solid-state NMR, and molecular dynamics, which showed chemical bonds between CO<sub>2</sub> and the amino groups.

<sup>a</sup>Department of Chemistry, Faculty of Science and Engineering, Swansea University, Grove Building, Singleton Park, Swansea, SA2 8PP, UK. E-mail: mariolino.cart@swansea.ac.uk

<sup>b</sup>Department of Chemical and Pharmaceutical Sciences, CENMAT, Centre of Excellence for Nanostructured Materials, INSTM Udr Trieste, University of Trieste, Via Licio Giorgieri 1, Trieste, 34127, Italy. E-mail: prato@units.it; jacopo.dosso@units.it

<sup>c</sup>Department of Chemistry, Northwestern University, Evanston, Illinois, 60208, USA

<sup>d</sup>Institute on Membrane Technology, National Research Council of Italy (CNR-ITM), Via P. Bucci 17/C, Rende, CS, 87036, Italy. E-mail: alessio.fuoco@cnr.it

<sup>e</sup>Department of Physics and CNR-Nanotec, University of Calabria, Rende, 87036, Italy

<sup>f</sup>Centre for Cooperative Research in Biomaterials (CIC BiomaGUNE), Basque Research and Technology Alliance (BRTA), Paseo de Miramón 194, Donostia San Sebastián, 20014, Spain

<sup>g</sup>Basque Fdn Sci, Ikerbasque, Bilbao, 48013, Spain

† Electronic supplementary information (ESI) available. See DOI: <https://doi.org/10.1039/d5ta02477c>

Beyond gas separation, Song's<sup>18</sup> group engineered spirobifluorene-based PIMs to incorporate sulfonic acid in the repeat units, resulting in a significant improvement in redox flow battery performance. Building on this, stimuli-responsive structural modifications could further enhance PIM selectivity and transport properties. In fact, despite a growing number of works reporting new types of PIMs with continuously improved properties, the concept of introducing responsive units in such materials is still underexplored, with most examples focusing on using light as stimulus.<sup>4,19</sup> Indeed, building PIMs functionalized with redox responsive molecular switches could produce materials that can change their properties "on demand". By employing chemical or electrical stimuli these changes could lead to the tuning of their porosity, their polarity and charge, and their gas selectivity, all parameters that may greatly affect the final properties of a material.<sup>14,15</sup> Building on this idea, we recently reported the development and reversible molecular switching of symmetrically  $\pi$ -extended dihydrophenazines.<sup>20,21</sup> These molecules can be easily oxidized to their aromatic dicationic form, which is permanent once induced but can be reduced back to the neutral form by treatment with soft nucleophiles (e.g., Triphenylphosphine, Fig. 1A). Moreover, the oxidation to the dicationic form is also associated with a dramatic electrochromic and conformational switch, which can have important effects when introduced in porous networks.<sup>21</sup> Given the rigidity and contortion of these molecules, which are typical features of monomers that produce high performing PIMs,<sup>22</sup> and the relative ease of functionalization with catechol units (Fig. 1B),<sup>9</sup>  $\pi$ -extended dihydrophenazines can be ideal candidates for the synthesis of redox switchable PIMs, especially exploiting nucleophilic aromatic substitutions as the polymerization reaction, which is typical of polybenzodioxin-based PIMs<sup>22</sup> (Fig. 1C).

As such, in this work we report the first synthesis and complete characterization of  $\pi$ -extended dihydrophenazine based PIMs. These materials present promising properties and

can be reversibly oxidized and reduced, resulting in an increased selectivity between CO<sub>2</sub> and N<sub>2</sub> upon oxidation.

## 2. Results and discussion

### 2.1 Synthesis of polymeric materials

Building on our previous work on  $\pi$ -extended dihydrophenazine systems,<sup>20,21</sup> we sought to utilize the presence of catechol moieties<sup>9</sup> and the rigid contorted nature of these backbones to synthesize polybenzodioxin-based polymers of intrinsic microporosity. We deem this investigation to be particularly significant because, as demonstrated in prior studies,<sup>21</sup> the dihydrophenazine backbone can be reversibly oxidized to its aromatic dicationic form, which leads to a conformational change that could potentially modify the microporosity of the material. In fact, based on a qualitative assessment of previously published X-Ray diffraction (XRD) crystal structures (Fig. 1A),<sup>21</sup> we believe this change results in a more rigid and contorted arrangement, characteristic of highly porous PIMs,<sup>13</sup> which may impact gas uptake, diffusion and release when used as a gas separation material. Herein we exploit this reversibility but within the polymeric chains, and not just on discrete molecules, to assess whether the expected changes also produce an alteration of the textural properties of the materials, such as porosity and pore size distribution (PSD). More specifically, we characterized the polymers in their initial pristine state (before oxidation, Fig. 2A), after oxidation of the dihydrophenazine system (Fig. 2B), and following its subsequent reduction to go back to the original form. In this way we aimed to confirm the polymers' ability to fully recover its initial properties, effectively demonstrating a chemo-switchable material. Building on previous findings about the irreversible structural changes in oxidized dihydrophenazine when exposed to nucleophilic molecules such as H<sub>2</sub>O, we also investigated how this degradation occurs within the polymer (Fig. 2C), aiming for a deeper understanding of the associated properties changes. This study is particularly focused on evaluating the potential of this chemo-switchable material for applications such as carbon capture and gas separation. In particular, any alterations in porosity and pore size distribution during oxidation–reduction cycles could significantly impact the

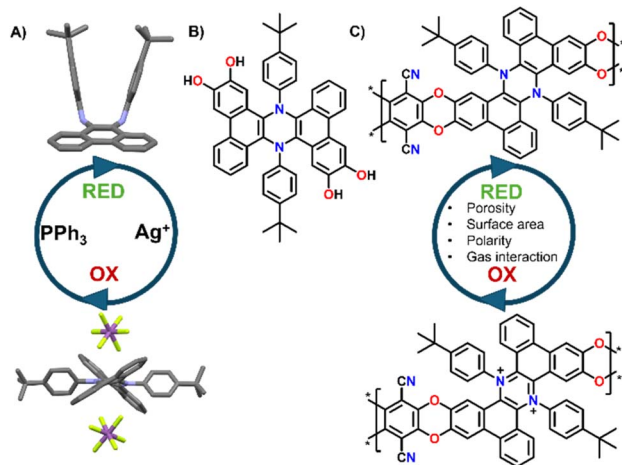


Fig. 1 (A) Parent  $\pi$ -extended dihydrophenazine chemical oxidation/reduction cycle; (B) catechol functionalized derivatives; (C) proposed structure of the switchable  $\pi$ -extended dihydrophenazine based PIMs.

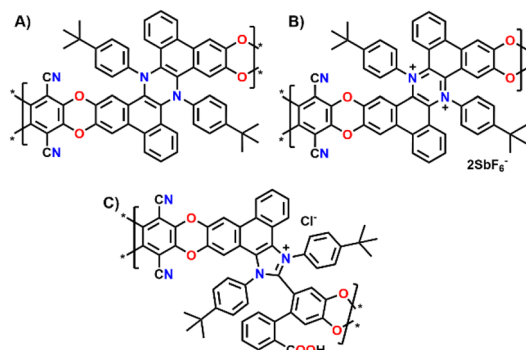


Fig. 2 Structures of the three different versions of (A) Phen-PIM-1; (B) Phen-PIM-1<sup>ox</sup>; and (C) Phen-PIM-1<sup>deg</sup>.

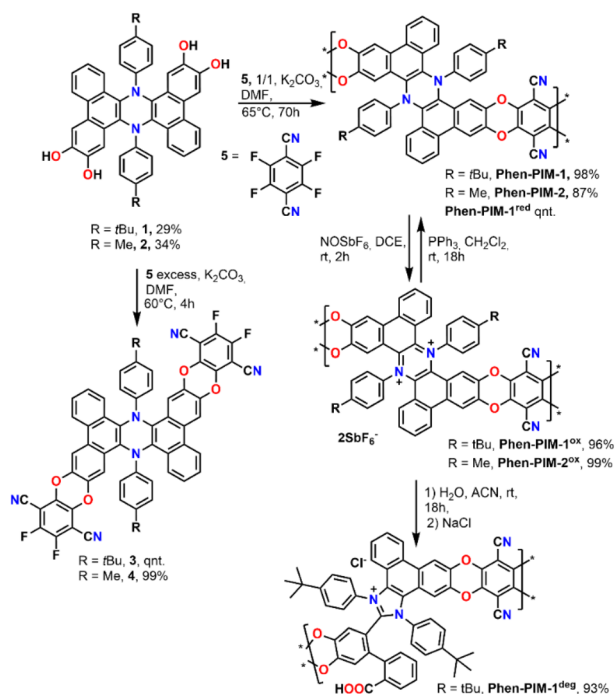


permeability and selectivity of the polymers for commercially important gas pairs, especially  $\text{CO}_2/\text{N}_2$ . These insights are crucial for assessing their suitability in separation technologies.

We started the synthesis by preparing dihydrophenazine biscatechol **1** (Scheme 1) following a procedure reported in our previous contribution.<sup>9</sup> Since these substrates were never used in combination with tetrafluoroterephthalonitrile **5**, which is one of the most common fluorinated monomers used for the synthesis of PIMs, the reaction conditions were initially tested on **1** using an excess of **5** in the presence of  $\text{K}_2\text{CO}_3$  in anhydrous DMF at 60 °C. As a result, the fluorinated monomeric unit **3** was obtained in a quantitative yield. Derivative **3** proved to be soluble enough in chlorinated solvents to be completely characterized using nuclear magnetic resonance spectroscopy (1D and 2D NMR). Moreover, the monomeric units presented a marked visible absorption in the 350–450 nm region of the spectra as typically associated with the introduction of oxygen atoms on the phthalonitrile system (Fig. S31†). The efficient preparation of model compound **3** confirmed that the same conditions would work in the polymerization and that the dihydrophenazine would not hinder it. Thus, **1** was treated with an equimolar amount of **5** in the presence of  $\text{K}_2\text{CO}_3$  in anhydrous and degassed DMF at 65 °C for 70 h (Scheme 1). The long reaction time was used to ensure complete reaction of the starting materials, and the formation of long polymeric chains.<sup>23</sup> As a result, a dense bright yellow solid was formed, which was extensively purified by washing with several solvents (Section 2.6 in the ESI†) to ensure removal of short oligomers

and salts and affording **Phen-PIM-1** as a dark yellow solid in almost quantitative yield.

To assess the effects on the material properties of the *tert*-butyl group (*t*Bu), the same synthetic strategy was repeated with methyl functionalized dihydrophenazine **2**, resulting in the formation of **Phen-PIM-2**. We anticipated that the presence of the *t*Bu groups may slightly reduce the porosity compared to the methyl version, by a pore filling effect.<sup>24</sup> However, the larger aliphatic *t*Bu groups are also expected to enhance the solubility in organic solvents.<sup>25</sup> To test the feasibility of the oxidation reaction on the system, monomer **3** was treated with an excess of  $\text{NOSbF}_6$  as an oxidant, resulting in the formation of a deep green solution (Section 2.3 in the ESI†). NMR analysis of the green solid highlighted the presence of a closed shell system fully consistent with the quantitative formation of dicationic  $3^{2+}$  (Fig. S15–S17†). Moreover, a UV-vis investigation highlighted a profile also compatible with the formation of the dicationic system (Fig. S31†) in line with previously reported examples. Based on this, the same reaction was then carried out on the two polymers to generate their oxidized form. As such, **Phen-PIM-1** and **Phen-PIM-2** were suspended in dichloroethane (DCE) and treated with a slight excess of  $\text{NOSbF}_6$  (Sections 2.7 and 2.8 in the ESI†). As a result, an immediate color change of the solids was visible and after purification **Phen-PIM-1<sup>ox</sup>** and **Phen-PIM-2<sup>ox</sup>** could be isolated in almost quantitative yield. To assess the reversible nature of the transformation, **Phen-PIM-1<sup>ox</sup>** was then also treated with  $\text{PPh}_3$  which is known to reversibly reduce the dicationic form to the initial neutral one, resulting in quantitative formation of **Phen-PIM-1<sup>red</sup>**. Finally, a batch of **Phen-PIM-1<sup>ox</sup>** was also treated with  $\text{H}_2\text{O}$  in acetonitrile (ACN) solution, which, as expected based on previous reports by our group,<sup>21</sup> resulted in the irreversible degradation of the material generating **Phen-PIM-1<sup>deg</sup>**.



Scheme 1 Synthetic procedure for the preparation of dihydrophenazine models (**3** and **4**), **Phen-PIM-1** and **Phen-PIM-2** and their oxidation, reduction, and degradation.

## 2.2 Characterization of PIMs

**2.2.1 Structural assessment.** The thermal stability of the polymeric samples was assessed *via* thermogravimetric analysis (TGA, Fig. S33†). In addition, this technique allows the evaluation of the conversion of the pristine material into its oxidized form by monitoring the loss of the  $\text{SbF}_6^-$  counter-anion. In its completely oxidized form, **Phen-PIM-1<sup>ox</sup>** (orange trace in Fig. S33†) contains approximately 35% of  $\text{SbF}_6^-$ . A step corresponding to a mass loss of ~28% with an onset temperature of 250 °C, which can be attributed to the loss of the counter-anion, can be readily observed as it is distinctly separated from the final decomposition step, which occurs at ~460 °C similarly to that of the pristine material, allowing for clear identification of the oxidation product. Given the relative accuracy of this method, which involved a temperature increase ramp of 10 °C  $\text{min}^{-1}$ , the experimental value indicates that 80% of the polymer backbone was successfully oxidized. Notably, the oxidized product could be effectively reverted to its original form (grey trace in Fig. S33†), as can be observed by its restored TGA curve which closely resembles that of the pristine material. Finally, the irreversible degradation into **Phen-PIM-1<sup>deg</sup>** elucidated in our previous work,<sup>21</sup> which was also confirmed as the



theoretical loss of 4.1% corresponding to the mass of the chloride counter-anion, aligns closely with the  $\sim 5\%$  step observed experimentally (purple trace in Fig. S33†).

Due to the lack of solubility in common deuterated solvents, typically used for solution NMR, the **Phen-PIMs** structures were characterized by FT-IR (Fig. S32†) and  $^{13}\text{C}$  solid-state-NMR (ssNMR, Fig. S22–S27†). In Fig. 3, we display the ssNMR spectra of the two forms of **Phen-PIM-1**: the original (black trace) and the oxidized (purple), and we observe that all expected peaks are present and consistent with previously reported structures of similar phenazines. Although the two spectra appear rather similar, subtle differences are also evident, suggesting that the transformation of the original **Phen-PIM-1** into its oxidized form has occurred.<sup>21</sup> Specifically, the peaks at  $\sim 30$ – $33$  ppm, which can be readily attributed to the *t*Bu substituents, in the oxidized form (purple) are slightly shifted to a lower field compared to the original (black). The signal at  $\sim 94$  ppm, likely assigned to the carbon linked to the nitrile group, remains in the same position as it is distant from the nitrogen.<sup>26</sup> The aromatic region peaks are overlapped and difficult to assign precisely, but they are consistent with the reported structures, and the peaks at  $\sim 139$ – $142$  ppm show a slight shift and change in shape. Also, comparing the  $^{13}\text{C}$  ssNMR of **Phen-PIM-1** and **Phen-PIM-1<sup>ox</sup>** with the solution  $^{13}\text{C}$  NMR of the monomeric units **3** and **3<sup>2+</sup>** highlights an excellent correspondence between signals, suggesting the presence of very similar units in the materials. Finally, the signal centered at 167 ppm in **Phen-PIM-1<sup>deg</sup>**, which may be related to the COOH groups generated by the degradation (as confirmed by the degradation of **3<sup>2+</sup>**, see the ESI†), is not observed in **Phen-PIM-1<sup>ox</sup>**, which rules out the occurrence of extensive degradation in the latter and confirms the expected nature of the different polymers.

**2.2.2 Textural and morphological characterization.** Analysis of the samples by scanning electron microscopy (SEM) revealed similar morphologies across all **Phen-PIM** samples (Fig. 4), characterized by highly amorphous polymers with no discernible average dimensions. No significant differences were observed between the original and oxidized forms, indicating

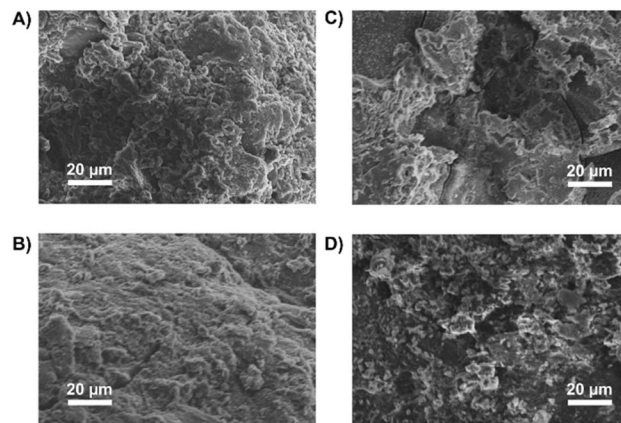


Fig. 4 SEM images of the Phen-PIMs: (A) Phen-PIM-1 pristine; (B) Phen-PIM-1<sup>ox-red</sup>; (C) Phen-PIM-1<sup>ox</sup>; (D) Phen-PIM-1<sup>deg</sup>.

that particle size and morphology remain unchanged during the oxidation and reduction processes.

As anticipated from the contorted structure of the monomers, both **Phen-PIM-1** (Fig. 2A) and **Phen-PIM-2** exhibited the high porosity characteristic of high-performing PIMs.<sup>22,23</sup> The methyl functionalized polymer (**Phen-PIM-2**) proved to be only slightly more porous, with a  $\text{S}_{\text{BET}}$  of  $633 \text{ m}^2 \text{ g}^{-1}$ , compared to  $618 \text{ m}^2 \text{ g}^{-1}$  for the *t*Bu version (**Phen-PIM-1**), as determined by nitrogen adsorption at 77 K. This was expected due to the pore filling effect of the *t*Bu group,<sup>24</sup> as already mentioned. Nevertheless, the difference is not particularly significant, which confirms that also **Phen-PIM-1** is highly microporous. Upon oxidation, both materials demonstrated a substantial reduction in porosity, likely due to the incorporation of the bulky  $\text{SbF}_6^-$  counter-anion, which is expected to occupy the pores and significantly reduce the initial free volume associated with the inefficient packing typical of PIMs, by generating an even more pronounced pore filling.<sup>27</sup> Because of that, the kinetics of nitrogen adsorption at 77 K proved to be significantly slow, resulting in negligible surface area measurements (Table 1). The pronounced hysteresis observed in the adsorption isotherms (see Fig. S36 and S37†), however, indicated that the materials retained some degree of porosity, and suggests the presence of inaccessible or partially buried pores that are difficult for the relatively large  $\text{N}_2$  probe gas to penetrate. To address this limitation, as reported in previous studies,<sup>11</sup> and to more properly assess the intrinsic porosity of these samples, carbon dioxide adsorption isothermal measurements at 273 K were performed. In fact, the smaller molecular size of  $\text{CO}_2$  and the higher temperature of adsorption enhance diffusion and grant access to smaller pores.<sup>28</sup> Indeed, these measurements confirmed that the oxidized PIMs remained porous, with surface areas of  $244 \text{ m}^2 \text{ g}^{-1}$  for **Phen-PIM-2<sup>ox</sup>** and  $321 \text{ m}^2 \text{ g}^{-1}$  for the *t*Bu-functionalized polymer (**Phen-PIM-1<sup>ox</sup>**, Fig. 2B), calculated *via* the Grand Canonical Monte Carlo (GCMC) method.<sup>28</sup> Interestingly, in contrast to **Phen-PIM-2<sup>ox</sup>**, in this case the *t*Bu-functionalized variant exhibited slightly higher porosity. As previously anticipated, **Phen-PIM-1** was also subjected to irreversible degradation, a process initially observed in the

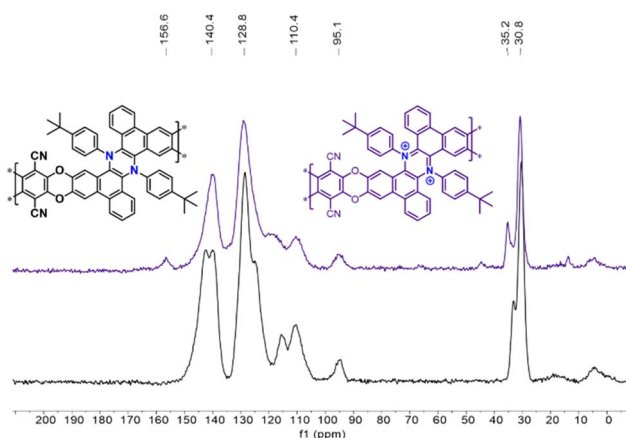


Fig. 3  $^{13}\text{C}$  ssNMR of Phen-PIM-1 (black trace) and Phen-PIM-1<sup>ox</sup> (purple trace).



Table 1 Textural properties of Phen-PIMs

Polymer	BET ( $\text{m}^2 \text{g}^{-1}$ )	Pore volume <sup>a</sup> ( $\text{cc g}^{-1}$ )	CO <sub>2</sub> adsorption		Selectivity <sup>b</sup>	
			273 K (1 bar) ( $\text{cc g}^{-1}$ ) (mmol g <sup>-1</sup> )	298 K (1 bar) ( $\text{cc g}^{-1}$ ) (mmol g <sup>-1</sup> )	CO <sub>2</sub> /N <sub>2</sub>	Q <sub>st</sub> <sup>c</sup> (kJ mol <sup>-1</sup> )
This work						
<b>Phen-PIM-2</b>	633 (509) <sup>a</sup>	$4.473 \times 10^{-1}$	51 (2.28)	32 (1.41)	38	30.9
<b>Phen-PIM-1</b>	618 (501) <sup>a</sup>	$5.620 \times 10^{-1}$	55 (2.45)	38 (1.70)	49	29.1
<b>Phen-PIM-2<sup>ox</sup></b>	1.7 (244) <sup>a</sup>	$(7.460 \times 10^{-2})^a$	25 (1.12)	19 (0.85)	61	29.9
<b>Phen-PIM-1<sup>ox</sup></b>	1.05 (321) <sup>a</sup>	$(1.127 \times 10^{-1})^a$	32 (1.43)	21 (0.94)	64	32.2
<b>Phen-PIM-1<sup>deg</sup></b>	246 (377) <sup>a</sup>	$1.887 \times 10^{-1}$	43 (1.92)	26 (1.16)	42	32.9

<sup>a</sup> BET values from adsorption of N<sub>2</sub> at 77 K. In parentheses the surface areas calculated from CO<sub>2</sub> @273 K using the GCMC method.<sup>28</sup> <sup>b</sup> Selectivity calculated according to IAST at 298 K and 1 bar.<sup>10,29</sup> <sup>c</sup> Isothermic heat of adsorption (Q<sub>st</sub> in kJ mol<sup>-1</sup>) of the corresponding gas at zero coverage calculated from isotherms collected at 273 and 298 K and fitted with the Langmuir-Freundlich equation and calculated *via* the Clausius Clapeyron equation.

phenazine-backbone in the original study.<sup>21</sup> The resulting **Phen-PIM-1<sup>deg</sup>** (Fig. 2C) showed intermediate porosity, with a surface area of  $246 \text{ m}^2 \text{g}^{-1}$  calculated from the N<sub>2</sub> isotherm measured at 77 K, and  $377 \text{ m}^2 \text{g}^{-1}$  when evaluated with CO<sub>2</sub> at 273 K. This result aligns with expectations, as the chain rearrangements hinder efficient packing, and the counter-anion can be exchanged from SbF<sub>6</sub><sup>-</sup> to the less bulky chloride counter-anion. Pore volume calculations, determined using both N<sub>2</sub> and CO<sub>2</sub> adsorption, confirmed that all polymers possessed substantial free volume, ranging from  $7.460 \times 10^{-2}$  to  $5.620 \times 10^{-1} \text{ cc g}^{-1}$  (Table 1). A high free volume is obviously crucial for applications such as gas separation, as will be discussed later. A key aspect of this study is represented by the reversibility of the porosity of the samples when subjected to oxidation and subsequent reduction, and this represents one of the most intriguing and distinctive properties of the new **Phen-PIMs**. As discussed, and shown in Fig. S37,† the oxidation of **Phen-PIM-1** leads to the expected decrease in adsorption and, consequently, in surface area. However, upon reduction, adsorption measurements revealed nearly identical isothermal curves and surface area calculations to those observed prior to oxidation (Fig. 5A). This demonstrates that the porosity can be effectively restored, highlighting the material's ability to undergo cycles of oxidation and reduction while retaining its original performance.

The PSD of **Phen-PIMs** was assessed *via* CO<sub>2</sub> adsorption at 273 K, with calculations performed *via* the Non-Local Density Functional Theory (NLDFT) method. The graph presented in Fig. 5B reveals a PSD typical of PIMs,<sup>30</sup> featuring an initial set of peaks centered at 3–4 Å, corresponding to the ultra-microporous region, a broader range between 4.5 and 7 Å, and a final tail centered around 7–10 Å. The reduction in surface area following the oxidation of the **Phen-PIM** backbone is also reflected in the changes to the pore size distribution. Specifically, the peaks of the oxidized versions are significantly diminished (see Fig. S39† for a full comparison), whereas the irreversibly modified polymer exhibits an intermediate PSD. Importantly, Fig. 5B also demonstrates the complete reversibility of the PSD upon oxidation and subsequent reduction, as the two traces overlap almost perfectly.

**2.2.3 CO<sub>2</sub> uptake, heats of adsorption and CO<sub>2</sub>/N<sub>2</sub> IAST selectivity.** All **Phen-PIMs** exhibited significant carbon dioxide uptake at both 273 K and 298 K (Table 1). The *t*Bu derivative showed slightly higher adsorption ( $2.45 \text{ mmol g}^{-1}$  at 273 K and  $1.70 \text{ mmol g}^{-1}$  at 298 K) compared to the methyl counterpart ( $2.28 \text{ mmol g}^{-1}$  at 273 K and  $1.41 \text{ mmol g}^{-1}$  at 298 K), although the values are very similar within the margin of error typical of these measurements. Despite the slightly lower surface area, we attribute the enhanced CO<sub>2</sub> uptake of the *t*Bu version to the higher amount of pores centered at  $\sim 4.5\text{--}7 \text{ Å}$ , which we attribute to the narrowing of the pore size induced by the *t*Bu groups (Fig. S40†). The oxidized forms followed the same trend but exhibited lower overall uptake, likely due to the reduced porosity of the samples. Notably, despite the significant decrease in surface area upon oxidation, the CO<sub>2</sub> uptake remained relatively high ( $1.43 \text{ mmol g}^{-1}$  at 273 K and  $0.94 \text{ mmol g}^{-1}$  at 298 K for **Phen-PIM-1<sup>ox</sup>**), which shows good affinity for this gas. Consistent with the surface area trends, **Phen-PIM-1<sup>deg</sup>** exhibited intermediate CO<sub>2</sub> uptake values, falling between those of the pristine and oxidized forms. Measurements of CO<sub>2</sub> adsorption at different temperatures also allowed for the calculation of the isosteric heats of adsorption (Q<sub>st</sub>, Table 1 and Fig. S41†). Interestingly, all samples exhibited remarkably similar Q<sub>st</sub> values ( $\sim 30 \text{ kJ mol}^{-1}$ ), despite the

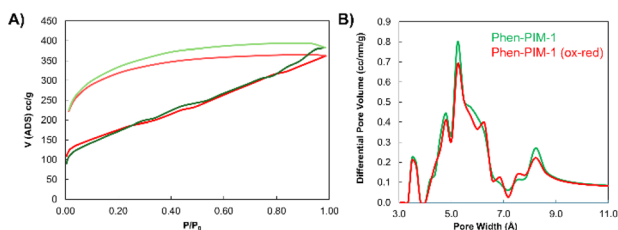


Fig. 5 (A) N<sub>2</sub> isotherms for **Phen-PIM-1** original (green) and after oxidation/reduction (red). The lighter curves represent the desorption pathway; (B) pore size distribution calculated from CO<sub>2</sub> adsorption at 273 K and *via* NLDFT. Color code original (green) vs. oxidation/reduction (red).



expectation that the oxidized forms, with their permanent positive charge on the nitrogen atoms, would show a higher affinity for CO<sub>2</sub>. This unexpected result suggests the existence of a trade-off between the increased electrostatic interactions provided by the charged nitrogen atoms, and the reduced surface areas of the oxidized samples. This balance appears to mitigate differences in adsorption behavior, resulting in comparable heats of adsorption across all samples and indicating a similar overall affinity for CO<sub>2</sub>. Following the CO<sub>2</sub> adsorption measurements at 298 K, nitrogen adsorption was also conducted at the same temperature to evaluate the ideal selectivity of these materials for potential application in post-combustion separation processes.<sup>31,32</sup> Using the IAST++ software,<sup>29</sup> the adsorption curves were fitted with the IAST method to calculate the ideal selectivity, assuming a 15% CO<sub>2</sub> and 85% N<sub>2</sub> gas mixture, representative of typical flue gas compositions during post-combustion carbon capture.<sup>33</sup> The oxidized polymer achieved a selectivity exceeding 60, while the original **Phen-PIMs** afforded values ranging between 38 and 49. This can be attributed to the reduced pore size in the oxidized form that, despite allowing less CO<sub>2</sub> to pass through, blocks even more efficiently the larger N<sub>2</sub> molecules, thereby enhancing selectivity. As observed previously, the degraded sample exhibited intermediate performance, reinforcing the consistency of the system. It is worth noting that, although the oxidized form demonstrated higher selectivity, its limited porosity makes the original polymer more practical for applications requiring the processing of larger gas volumes as its higher flux capacity enables the treatment of greater amounts of gas simultaneously.

As anticipated, the presence of the *t*Bu groups had the effect of increasing polymer solubility. In fact, while **Phen-PIM-2** was poorly soluble in all solvents, **Phen-PIM-1** was soluble in *N*-methyl pyrrolidone (NMP), which allowed the casting of a robust film, suitable for the evaluation of its properties for potential applications as membranes for gas separation.

Moreover, it is worth mentioning that the limited solubility of the oxidized form, **Phen-PIM-1<sup>ox</sup>**, prevented the formation of a stable film. As a result, the selectivity comparison between the two forms is based on the powder form using IAST calculations, as shown in Table 1. The pristine **Phen-PIM-1** film was insoluble in methanol, which could therefore be used for the standard soaking and drying treatment typically employed to remove traces of residual casting solvent from PIM films and to reverse the effect of physical aging.<sup>34,35</sup> Unfortunately, the scarce solubility of the methyl counterpart (**Phen-PIM-2**) prevented its gas permeability evaluation and, so, a full comparison of the two new PIMs. The order of gas permeability for **Phen-PIM-1** is CO<sub>2</sub> > H<sub>2</sub> > He > O<sub>2</sub> > CH<sub>4</sub> > N<sub>2</sub> (Table 2); this is half way between the trend of the ultra-permeable PIMs, in which CO<sub>2</sub> has a higher permeability than H<sub>2</sub>,<sup>25,36,37</sup> and the typical trend of PIMs with very high diffusivity selectivity, in which He has a higher permeability than O<sub>2</sub>.<sup>38–40</sup> The size-sieving character of **Phen-PIM-1** is highlighted by the steep correlation between the diffusion coefficient and the squared effective diameter of the gas with a slope increase for the aged film (Fig. S43†). The slope increase is usually associated with an increase of the Young's

**Table 2** Single gas permeability  $P_a$ , diffusivity  $D_a$ , and solubility  $S_a$ , coefficients of gas, and associated selectivity over N<sub>2</sub> for methanol treated and 211 day aged films of **Phen-PIM-1** measured at 25 °C and 1 bar feed pressure

Transport properties	Permeability, diffusivity and solubility					
	N <sub>2</sub>	O <sub>2</sub>	CO <sub>2</sub>	CH <sub>4</sub>	H <sub>2</sub>	He
$P_a$ [Barrer]	688.6	2628	12492	933.8	8254	3332
$\alpha$ ( $i/N_2$ )	(–)	(3.82)	(18.1)	(1.35)	(11.9)	(4.84)
Aged	356.8	1713	7994	470.6	6851	2868
$\alpha$ ( $i/N_2$ )	(–)	(4.80)	(22.4)	(1.31)	(19.2)	(8.04)
$D_a$ [ $10^{-12}$ m <sup>2</sup> s <sup>-1</sup> ]	105.6	383.5	136.0	38.8	– <sup>a</sup>	– <sup>a</sup>
$\alpha$ ( $i/N_2$ )	(–)	(3.63)	(1.29)	(0.36)	– <sup>a</sup>	– <sup>a</sup>
Aged	50.3	203	66.7	15.3	– <sup>a</sup>	– <sup>a</sup>
$\alpha$ ( $i/N_2$ )	(–)	(4.03)	(1.32)	(0.30)	– <sup>a</sup>	– <sup>a</sup>
$S_a$ [cm <sup>3</sup> <sub>STP</sub> cm <sup>-3</sup> bar <sup>-1</sup> ]	4.89	5.14	68.9	18.0	– <sup>a</sup>	– <sup>a</sup>
$\alpha$ ( $i/N_2$ )	(–)	(1.05)	(14.1)	(3.68)	– <sup>a</sup>	– <sup>a</sup>
Aged	5.32	6.31	89.9	23.0	– <sup>a</sup>	– <sup>a</sup>
$\alpha$ ( $i/N_2$ )	(–)	(1.19)	(16.9)	(4.32)	– <sup>a</sup>	– <sup>a</sup>

<sup>a</sup>  $D_a$  and  $S_a$  values for H<sub>2</sub> and He are not reported due to the fast membrane time-lag.

moduli of the film due to aging.<sup>41</sup> AFM force spectroscopy measurements were performed on both freshly methanol treated and aged samples in different positions, and the sampling scans show that the freshly treated sample has a narrow distribution of the Young's modulus with an average of  $1.79 \pm 0.12$  GPa (Fig. S44A†). Thus, this polymer proved to be stiffer with respect to PIM-1<sup>42</sup> but with similar Young's moduli or slightly more flexible than the ultrapermeable PIMs (Fig. S44B†).<sup>37,41</sup> The aged film shows a broader distribution, with two main peaks centered at  $3.01 \pm 0.16$  GPa and  $5.58 \pm 0.32$  GPa (Fig. S44A†). The aging trend is similar to what has been previously observed for other PIMs and the bimodal distribution can be associated with the fact that aging occurs predominantly at the surface of the film and this creates a concentration gradient of fractional free volume near the surface.<sup>41,43</sup>

The relative position of permeability and selectivity for selected gas pairs, which is displayed in the Robeson plot (Fig. 6), serves as a critical tool for researchers and engineers to evaluate and compare the efficiency of new membrane materials in gas separation applications, such as carbon capture and natural gas purification. Developed by L. M. Robeson in 1991, revised in 2008 for most of the commercially important gas pairs and then updated by other groups for specific separations,<sup>44–47</sup> the plot depicts the performance of various polymeric membranes for gas separation, with permeability on the x-axis and selectivity (often represented as the ratio of the permeabilities of two gases) on the y-axis. In our case, the CO<sub>2</sub> permeability of **Phen-PIM-1** proved to be similar to or higher than that of other *t*Bu containing PIMs (*i.e.*, PIM-SBF-5,<sup>40</sup> PIM-TOT-SBF-5,<sup>38</sup> and DPT-TMPD<sup>48</sup>). Its higher selectivity, however, places this  $\pi$ -extended dihydrophenazine-based PIM above the 2008 upper bound in a more interesting region of the Robeson plots (Fig. 6A and B), close to the requirements for high permeance/low-energy membranes for power plant post-



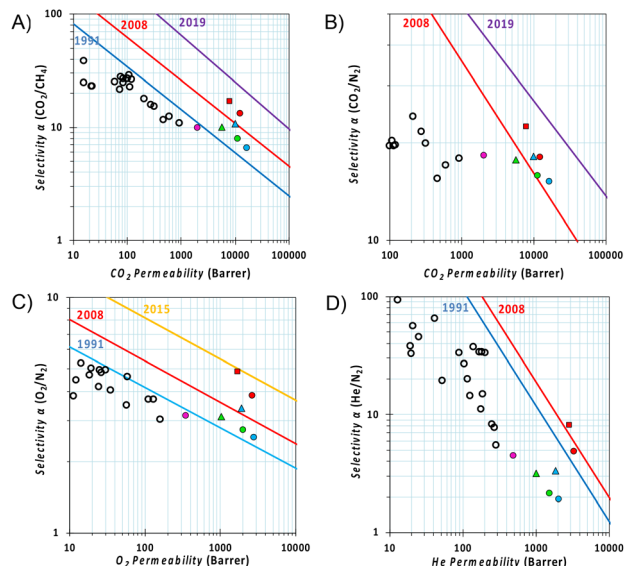


Fig. 6 Robeson diagrams for the (A)  $\text{CO}_2/\text{CH}_4$ ; (B)  $\text{CO}_2/\text{N}_2$ ; (C)  $\text{O}_2/\text{N}_2$ ; and (D)  $\text{He}/\text{N}_2$  gas pairs with the upper bounds represented by blue lines for 1991,<sup>44</sup> red lines for 2008,<sup>45</sup> yellow lines for 2015,<sup>47</sup> and purple lines for 2019.<sup>46</sup> The gas permeabilities are reported for **Phen-PIM-1** in red (circle ● fresh and square ■ 211 day aged), for PIM-SBF-5 in blue (circle ● fresh and triangle ▲ 1439 day aged),<sup>40</sup> for PIM-TOT-SBF-5 in green (circle ● fresh and triangle ▲ 543 day aged),<sup>38</sup> for DPt-TMPD in pink (circle ● fresh),<sup>48</sup> and empty black circles are data for low free volume polymers with pendant *t*Bu groups.<sup>48,50–56</sup>

combustion carbon dioxide capture foreseen by Merkel *et al.*<sup>49</sup> The high  $\text{O}_2/\text{N}_2$  and  $\text{He}/\text{N}_2$  selectivity (Fig. 6C and D) is a further indication that the separation is strongly dependent on a molecular sieving mechanism, as both  $\text{O}_2$  and especially  $\text{He}$  have a smaller kinetic diameter with respect to  $\text{N}_2$  although their solubilities are not so different in polymers. In comparison with traditional low free volume polymers containing *t*Bu groups,<sup>48,50–56</sup> the **Phen-PIM-1** shows 2–3 orders of magnitude higher permeability values, while maintaining a similar ( $\text{CO}_2/\text{CH}_4$ ,  $\text{O}_2/\text{N}_2$ ) or slightly lower ( $\text{CO}_2/\text{N}_2$ ) selectivity (Fig. 6), thus showing encouraging performance for gas separation application for biogas upgrading,  $\text{CO}_2$  capture from flue gas and  $\text{O}_2/\text{N}_2$  enrichment from air. In this work, we also investigated physical aging by repeating gas permeability experiments 211 days after the first measurements. Physical aging is a common phenomenon observed in highly microporous materials that are out of their thermodynamic equilibrium state, which in highly microporous polymers is characterized by the relaxation of the polymer's molecular chains, which leads to a reduction in internal free volume and, consequently, a decrease in permeability.<sup>57</sup> As shown in Fig. 6, the expected loss of free volume resulted in a relative decrease in permeability for all gas pairs, accompanied by an increase in selectivity. Notably, the reduction in permeability is effectively counterbalanced by enhanced selectivity, ensuring that the overall performance remains relatively unchanged on the Robeson plot. This further demonstrates the enhanced molecular sieving effect achieved through the use of the dihydrophenazine monomer.

### 3. Conclusions

In this work, we have successfully demonstrated the potential of  $\pi$ -extended dihydrophenazine scaffolds as versatile building blocks for the development of novel microporous polymers. This study represents one of the few examples of structural redox-switchable PIMs reported in the literature, further expanding the scope of functional materials in this class. Comprehensive characterization was carried out to assess the textural properties (surface area and pore size distribution), morphology (SEM), and chemical composition of the synthesized materials.

Our findings highlight a remarkable balance between porosity, pore size, and gas selectivity, making these materials highly promising for gas separation applications. The solubility of **Phen-PIM-1** in NMP enabled its processing into a self-standing membrane with mechanical properties in the range of other thin film forming materials, a crucial feature for practical implementation for gas separation. In contrast, the methyl-substituted counterpart **Phen-PIM-2** exhibited poor solubility that prevented direct comparison of their membrane gas separation performance. These findings, although unfortunate, emphasize the critical role of large aliphatic *t*Bu groups in enhancing solubility and facilitating the formation of robust films. Gas separation studies, conducted both in powder form (*via* IAST) and in membrane form (*via* time-lag measurements), revealed excellent separation performance. Notably, **Phen-PIM-1** showed gas transport properties that place it in a highly competitive region of the Robeson upper bound for key gas pair separations such as  $\text{CO}_2/\text{CH}_4$  and  $\text{CO}_2/\text{N}_2$ , demonstrating its strong potential for carbon capture applications. Additionally, its performance in  $\text{O}_2/\text{N}_2$  and  $\text{He}/\text{N}_2$  separations suggests an enhanced molecular sieving effect, further broadening its applicability in gas purification processes.

Beyond its gas separation capabilities, this work marks an important milestone in the integration of dihydrophenazine-based compounds into the PIM family. The reversible redox behavior of these materials offers a rare example of switchable PIMs, opening new avenues for the design of stimuli-responsive porous materials. Given their highly promising properties, these materials lay a strong foundation for future optimization and functionalization, paving the way for their practical implementation in energy and environmental applications.

### Data availability

The data that support the findings of this study are available in the ESI† of this article.

### Author contributions

The manuscript was written through contributions of all authors. All authors have given approval to the final version of the manuscript.



## Conflicts of interest

The authors declare no conflict of interest.

## Acknowledgements

J. D. kindly acknowledges FRA2024-2025 funded by the University of Trieste and Microgrants 2024 funded by Regione FVG (LR 2/2011, ART. 4). M. P. is the AXA-Chair for Bionanotechnology (2016–2026). This work was supported by the University of Trieste, INSTM, the Italian Ministry of Education MIUR (cofin Prot. 20228YFRNL), and la Agencia Estatal de Investigaciones through grant PID2022-140419OB-I00 funded by MCIN/AEI/10.13039/501100011033. M. V. and A. F. received funding from the European Union's Horizon Europe research and innovation program under grant agreement no. 101115488, within the EIC pathfinder project "Double-Active Membranes for a sustainable CO<sub>2</sub> – DAM4CO<sub>2</sub>" (HORIZON-EIC-2022-PATHFINDERCHALLENGES-01). C.G.B. and M.C. gratefully acknowledge UK Research and Innovation (UKRI) under the UK government's Horizon Europe funding guarantee [grant number 10083164] associated with DAM4CO<sub>2</sub>. The authors gratefully acknowledge Daniel M. Dawson and the University of St Andrews for the <sup>13</sup>C ssNMR service.

## Notes and references

- 1 A. G. Slater and A. I. Cooper, *Science*, 2015, **348**, aaa8075.
- 2 T. D. Bennett, F. X. Coudert, S. L. James and A. I. Cooper, *Nat. Mater.*, 2021, **20**, 1179–1187.
- 3 Y. Li, J. Brückel, M. Jereb, A. Zupanc, S. P. Hirvonen, S. Hietala, M. Kemell, Y. Wu, O. Fuhr, R. D. Jansen-van Vuuren, M. Carta and S. Bräse, *Adv. Funct. Mater.*, 2024, **34**, 2401957.
- 4 A. Gafiullina, B. P. Ladewig and J. Zhang, *ACS Appl. Polym. Mater.*, 2023, **5**, 1–30.
- 5 J. Zhou and B. Wang, *Chem. Soc. Rev.*, 2017, **46**, 6927–6945.
- 6 X. Liu, C. F. Liu, W. Y. Lai and W. Huang, *Adv. Mater. Technol.*, 2020, **5**, 1–20.
- 7 J. Wu, F. Xu, S. Li, P. Ma, X. Zhang, Q. Liu, R. Fu and D. Wu, *Adv. Mater.*, 2019, **31**, 1–45.
- 8 J. Dosso, H. Oubaha, F. Fasano, S. Melinte, J.-F. Gohy, C. E. Hughes, K. D. M. Harris, N. Demitri, M. Abrami, M. Grassi and D. Bonifazi, *Chem. Mater.*, 2022, **34**, 10670–10680.
- 9 G. Gentile, B. Bartolomei, J. Dosso, N. Demitri, G. Filippini and M. Prato, *Chem. Commun.*, 2023, **60**, 602–605.
- 10 A. L. Myers and J. M. Prausnitz, *AIChE*, 1964, **11**, 121–127.
- 11 A. R. Antonangelo, N. Hawkins, E. Tocci, C. Muzzi, A. Fuoco and M. Carta, *J. Am. Chem. Soc.*, 2022, **144**, 15581–15594.
- 12 S. Mondal, A. Hassan, S. A. Wahed, A. Kumar and N. Das, *ACS Appl. Polym. Mater.*, 2025, 1503–1512.
- 13 N. B. McKeown, *Polymer*, 2020, **202**, 122736.
- 14 H. S. Lau, A. Eugenia, Y. Weng and W. F. Yong, *Prog. Mater. Sci.*, 2024, **145**, 101297.
- 15 H. W. H. Lai, F. M. Benedetti, J. M. Ahn, A. M. Robinson, Y. Wang, I. Pinnau, Z. P. Smith and Y. Xia, *Science*, 2022, **375**, 1390–1392.
- 16 W. Han, C. Zhang, M. Zhao, F. Yang, Y. Yang and Y. Weng, *J. Membr. Sci.*, 2021, **636**, 119544.
- 17 C. Rizzuto, F. Nardelli, M. Monteleone, L. Calucci, C. G. Bezzu, M. Carta, E. Tocci, E. Esposito, G. De Luca, B. Comesana-Gándara, N. B. McKeown, B. Sayginer, P. M. Budd, J. C. Jansen and A. Fuoco, *J. Mater. Chem. A*, 2025, **13**, 17865–17876.
- 18 C. Ye, A. Wang, C. Breakwell, R. Tan, C. Grazia Bezzu, E. Hunter-Sellers, D. R. Williams, N. P. Brandon, P. A. A. Klusener, A. R. Kucernak, K. E. Jelfs, N. B. McKeown and Q. Song, *Nat. Commun.*, 2022, **13**, 3184.
- 19 D. Becker, N. Konnertz, M. Böhning, J. Schmidt and A. Thomas, *Chem. Mater.*, 2016, **28**, 8523–8529.
- 20 J. Dosso and M. Prato, *Chem.–Eur. J.*, 2023, **29**, e202203637.
- 21 J. Dosso, B. Bartolomei, N. Demitri, F. P. Cossío and M. Prato, *J. Am. Chem. Soc.*, 2022, **144**, 7295–7301.
- 22 N. B. McKeown, *Curr. Opin. Chem. Eng.*, 2022, **36**, 100785.
- 23 C. Pathak, A. Gogoi, A. Devi and S. Seth, *Chem.–Eur. J.*, 2023, **29**, e202301512.
- 24 J. Jeromenok and J. Weber, *Langmuir*, 2013, **29**, 12982–12989.
- 25 I. Rose, C. G. Bezzu, M. Carta, B. Comesana-Gándara, E. Lasseguette, M. C. Ferrari, P. Bernardo, G. Clarizia, A. Fuoco, J. C. Jansen, K. E. Hart, T. P. Liyana-Arachchi, C. M. Colina and N. B. McKeown, *Nat. Mater.*, 2017, **16**, 932–937.
- 26 B. Satilmis, M. Lanč, A. Fuoco, C. Rizzuto, E. Tocci, P. Bernardo, G. Clarizia, E. Esposito, M. Monteleone, M. Dendisová, K. Friess, P. M. Budd and J. C. Jansen, *J. Membr. Sci.*, 2018, **555**, 483–496.
- 27 A. Wang, C. Breakwell, F. Foglia, R. Tan, L. Lovell, X. Wei, T. Wong, N. Meng, H. Li, A. Seel, M. Sarter, K. Smith, A. Alvarez-Fernandez, M. Furedi, S. Guldin, M. M. Britton, N. B. McKeown, K. E. Jelfs and Q. Song, *Nature*, 2024, **635**, 353–371.
- 28 D. Lozano-Castelló, D. Cazorla-Amorós and A. Linares-Solano, *Carbon*, 2004, **42**, 1233–1242.
- 29 S. Lee, J. H. Lee and J. Kim, *Korean J. Chem. Eng.*, 2018, **35**, 214–221.
- 30 M. Tian, S. Roach, H. Fawcett, A. D. Burrows, C. R. Bowen and T. J. Mays, *Adsorption*, 2020, **26**, 1083–1091.
- 31 K. T. Leperi, R. Q. Snurr and F. You, *Ind. Eng. Chem. Res.*, 2016, **55**, 3338–3350.
- 32 R. Mobili, Y. Wu, C. X. Bezuidenhout, S. La Cognata, S. Bracco, M. Carta and V. Amendola, *RSC Sustainability*, 2024, 3345–3352.
- 33 H. Zhou, C. Rayer, A. R. Antonangelo, N. Hawkins and M. Carta, *ACS Appl. Mater. Interfaces*, 2022, **14**, 20997–21006.
- 34 P. M. Budd, N. B. McKeown, B. S. Ghanem, K. J. Msayib, D. Fritsch, L. Starannikova, N. Belov, O. Sanfirova, Y. Yampolskii and V. Shantarovich, *J. Membr. Sci.*, 2008, **325**, 851–860.
- 35 K. Nagai, A. Higuchi and T. Nakagawa, *J. Polym. Sci., Part B Polym. Phys.*, 1995, **33**, 289–298.



- 36 J. Chen, M. Longo, A. Fuoco, E. Esposito, M. Monteleone, B. Comesaña Gándara, J. Carolus Jansen and N. B. McKeown, *Angew. Chem., Int. Ed.*, 2023, **62**, 1–9.
- 37 C. G. Bezzu, A. Fuoco, E. Esposito, M. Monteleone, M. Longo, J. C. Jansen, G. S. Nichol and N. B. McKeown, *Adv. Funct. Mater.*, 2021, **31**, 1–10.
- 38 S. A. Felemban, C. G. Bezzu, B. Comesaña-Gándara, J. C. Jansen, A. Fuoco, E. Esposito, M. Carta and N. B. McKeown, *J. Mater. Chem. A*, 2021, **9**, 2840–2849.
- 39 R. Malpass-Evans, I. Rose, A. Fuoco, P. Bernardo, G. Clarizia, N. B. McKeown, J. C. Jansen and M. Carta, *Membranes*, 2020, **10**, 62–74.
- 40 C. G. Bezzu, M. Carta, M. C. Ferrari, J. C. Jansen, M. Monteleone, E. Esposito, A. Fuoco, K. Hart, T. P. Liyana-Arachchi, C. M. Colina and N. B. McKeown, *J. Mater. Chem. A*, 2018, **6**, 10507–10514.
- 41 M. Longo, M. P. De Santo, E. Esposito, A. Fuoco, M. Monteleone, L. Giorno, B. Comesaña-Gándara, J. Chen, C. G. Bezzu, M. Carta, I. Rose, N. B. McKeown and J. C. Jansen, *Ind. Eng. Chem. Res.*, 2020, **59**, 5381–5391.
- 42 C. R. Mason, L. Maynard-Atem, N. M. Al-Harbi, P. M. Budd, P. Bernardo, F. Bazzarelli, G. Clarizia and J. C. Jansen, *Macromolecules*, 2011, **44**, 6471–6479.
- 43 B. W. Rowe, S. J. Pas, A. J. Hill, R. Suzuki, B. D. Freeman and D. R. Paul, *Polymer*, 2009, **50**, 6149–6156.
- 44 L. M. Robeson, *J. Membr. Sci.*, 1991, **62**, 165–185.
- 45 L. M. Robeson, *J. Membr. Sci.*, 2008, **320**, 390–400.
- 46 B. Comesaña-Gándara, J. Chen, C. G. Bezzu, M. Carta, I. Rose, M. C. Ferrari, E. Esposito, A. Fuoco, J. C. Jansen and N. B. McKeown, *Energy Environ. Sci.*, 2019, **12**, 2733–2740.
- 47 R. Swaidan, B. Ghanem and I. Pinnau, *ACS Macro Lett.*, 2015, **4**, 947–951.
- 48 R. Sulub-Sulub, M. I. Loria-Bastarrachea, H. Vázquez-Torres, J. L. Santiago-García and M. Aguilar-Vega, *J. Membr. Sci.*, 2018, **563**, 134–141.
- 49 T. C. Merkel, H. Lin, X. Wei and R. Baker, *J. Membr. Sci.*, 2010, **359**, 126–139.
- 50 Z. Qiu, G. Chen, Q. Zhang and S. Zhang, *Eur. Polym. J.*, 2007, **43**, 194–204.
- 51 N. Belov, R. Chatterjee, R. Nikiforov, V. Ryzhikh, S. Bisoi, A. G. Kumar, S. Banerjee and Y. Yampolskii, *Sep. Purif. Technol.*, 2019, **217**, 183–194.
- 52 S. Sánchez-García, F. A. Ruiz-Treviño, M. J. Aguilar-Vega and M. G. Zolotukhin, *Ind. Eng. Chem. Res.*, 2016, **55**, 7012–7020.
- 53 D. Ayala, A. E. Lozano, J. De Abajo, C. García-Perez, J. G. De La Campa, K. V. Peinemann, B. D. Freeman and R. Prabhakar, *J. Membr. Sci.*, 2003, **215**, 61–73.
- 54 N. Esteban, M. Juan-y-Seva, C. Aguilar-Lugo, J. A. Miguel, C. Staudt, J. G. de la Campa, C. Álvarez and Á. E. Lozano, *Polymers*, 2022, **14**, 5517–5538.
- 55 M. Calle, Á. E. Lozano, J. G. De La Campa and J. De Abajo, *Macromolecules*, 2010, **43**, 2268–2275.
- 56 M. Calle, C. García, A. E. Lozano, J. G. De la Campa, J. De Abajo and C. Álvarez, *J. Membr. Sci.*, 2013, **434**, 121–129.
- 57 Z. X. Low, P. M. Budd, N. B. McKeown and D. A. Patterson, *Chem. Rev.*, 2018, **118**, 5871–5911.

